CERN Super Proton Synchrotron Radiation Environment and Related Radiation Hardness Assurance Implications

Kacper Biłko, Rubén García Alía, *Member, IEEE*, Diego Di Francesca, Ygor Aguiar, *Member, IEEE*, Salvatore Danzeca, Simone Gilardoni, Sylvain Girard, *Senior Member, IEEE*, Luigi Salvatore Esposito, Matthew Alexander Fraser, Giuseppe Mazzola, Daniel Ricci, Marc Sebban, and Francesco Maria Velotti

***Abstract*— The super proton synchrotron (SPS) is the second largest accelerator at CERN where protons are accelerated between 16 and 450 GeV/c. Beam losses, leading to the mixed-field radiation of up to MGy magnitude, pose a threat to the reliability of the electronic equipment and polymer materials located in the tunnel and its vicinity. In particular, in the arc sectors, where both main magnets and radiation sensors are periodically arranged, the total ionizing dose (TID) is of concern for the front-end electronics of a logarithmic position system (ALPS). The SPS is equipped with multiple radiation detection systems, such as beam loss monitors (BLMs), RadMons, and as of 2021, the distributed optical fiber radiation sensor (DOFRS) that combined all together provides a very comprehensive picture of both the TID spatial distribution and its time evolution. Within this study, the overview of measured 2021 and 2022 TID levels is presented, together with the demonstration of capabilities offered by the different radiation monitors. The DOFRS, supported by the passive radiophotoluminescence (RPL) dosimeter measurements, is used to assess the TID values directly at the electronic racks, which turned out to be reaching several tens of Gy/year, potentially affecting the ALPS lifetime.**

***Index Terms*— Accelerator, beam loss monitor (BLM), beam losses, CERN, electronics, FLUKA, mixed-field radiation, Monte Carlo, optical fiber, radiophotoluminescence (RPL), super proton synchrotron (SPS), total ionizing dose (TID).**

I. Introduction

A DEEP understanding of the radiation environment is one of the key ingredients of radiation hardness assurance (RHA) in high-energy accelerators [1]. Therefore, the knowledge about radiation levels in the various accelerator locations hosting active electronics is critical in order to do the following: 1) mitigate possible radiation-induced failures, mainly through relocation and shielding and 2) define radiation tolerance requirements for accelerator systems under development.

An example of a high-energy and high-intensity accelerator where a mixed-field radiation environment affects electronic systems is the super proton synchrotron (SPS), the second largest accelerator at CERN, which supplies beam to experiments (AWAKE [2], HiRadMat [3], Fixed Target [4], and the Large Hadron Collider (LHC) [5]). Most of the time the accelerator is operated with the proton beam accelerated between momenta of 16 GeV/c (typically injection energy) and 450 GeV/c (extraction energy for LHC beams). With such high energies and beam intensities of $\sim 10^{13}$ protons, even small beam losses can lead to a severe radiation environment.

This calls for a profound knowledge of the radiation environment and prompt detection of any abnormal increase when compared with expected values. Such an increase could be dangerous for both electronic equipment installed in the accelerator and its surroundings and for personnel due to residual radiation. For this reason, multiple radiation monitors have been distributed along the 7-km SPS ring. Currently, the main dosimetry system, deployed in 2021, is the distributed optical fiber radiation sensor (DOFRS) [6], covering the entire accelerator and providing high spatial resolution of total ionizing dose (TID) measurements. Given the spatial coverage, the system is one-of-a-kind, with potential applications beyond the accelerator environments. This is the first work that exploits its radiation measurements collected in the SPS accelerator (so far the highest spatial coverage). Prior to 2018, the TID along the SPS was assessed by the radiophotoluminescence (RPL) dosimeters [7]. In addition, radiation levels in the SPS are measured using the beam loss monitors (BLMs) [8] and the RadMon detectors [9], [10].

This work presents an overview of the general radiation environment in the SPS accelerator, focusing on the arc sectors due to their periodic magnet and monitor arrangement. It also demonstrates the combined use of multiple types of radiation monitors to extract information not only about the radiation spatial profile but also the radiation-driving mechanism.

Although the SPS radiation environment had been studied from the losses [11], [12], [13] and the machine activation point of view [14], [15], to the best of our knowledge,

Manuscript received 14 October 2022; revised 16 February 2023; accepted 21 March 2023. Date of publication 23 March 2023; date of current version 16 August 2023.

Kacper Biłko is with CERN, 1211 Geneva, Switzerland, and also with Université de Saint-Etienne, Laboratoire Hubert Curien, UMR CNRS 5516, 42000 Saint-Etienne, France (e-mail: kacper.bilko@cern.ch).

Rubén García Alía, Diego Di Francesca, Ygor Aguiar, Salvatore Danzeca, Simone Gilardoni, Luigi Salvatore Esposito, Matthew Alexander Fraser, Giuseppe Mazzola, Daniel Ricci, and Francesco Maria Velotti are with CERN, 1211 Geneva, Switzerland.

Sylvain Girard and Marc Sebban are with Université de Saint-Etienne, Laboratoire Hubert Curien, UMR CNRS 5516, 42000 Saint-Etienne, France.

Color versions of one or more figures in this article are available at https://doi.org/10.1109/TNS.2023.3261181.

Digital Object Identifier 10.1109/TNS.2023.3261181

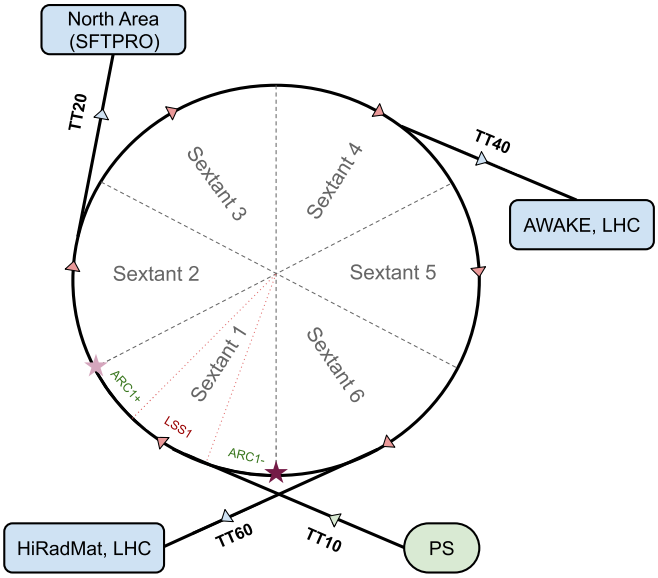

Fig. 1. Schematic of the SPS with both injection (TT10) and extraction transfer lines (TT20, TT40, and TT60).

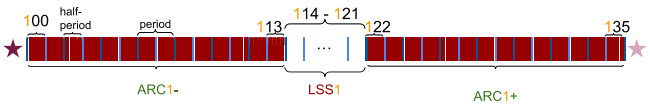

Fig. 2. Schematic of Sextant 1 with highlighted half-periods that limit ARC1−, LSS1, and ARC1+. The same naming convention is applicable to all Sextants. The stars at the beginning of ARC1− and at the end of ARC1+ correspond to the locations marked in Fig. 1.

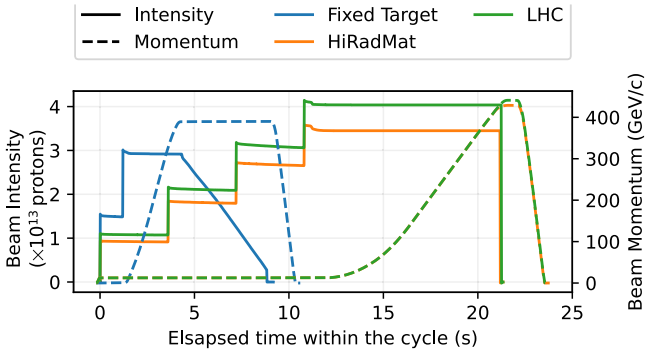

Fig. 3. Examples of the SPS cycles, in terms of beam intensity and beam momentum, for the most common beam users: North Area experiments (SFTPRO), LHC, and HiRadMat experiment. The SFTPRO beam is extracted in a slow manner (over multiple turns), whereas for the other users, the fast extraction takes place (single turn).

this is the first paper that provides a comprehensive analysis of the prompt radiation levels (during the operation), focusing on risks concerning the installed and future electronic systems. An example of such are front-end field-programmable gate array (FPGA) boards of a logarithmic position system (ALPS) [16], commercial-off-the-shell (COTS)-based, installed directly under the accelerator's magnets, or the SPS access system, containing industrial Siemens programmable logic controller (PLC) I/O cards, that despite not being installed in the direct proximity of the SPS beamline, was affected by the radiation failures during the 2021 operation [17].

This article is structured as follows. Section II presents an overview of the SPS in terms of the accelerator's layout (see Section II-A), the typical operation (see Section II-B), the deployed radiation sensors (see Section II-C), and the main prompt radiation sources (see Section II-D), i.e., beam loss mechanisms. Focusing on the arc sectors, Section III describes the TID measurements, and Section IV highlights the detection capabilities and limitations of the radiation monitors, focusing on the applications related to electronic equipment protection. Section V summarizes the studies with the RHA considerations.

II. Super Proton Synchrotron

A. Accelerator Layout

The SPS is a circular accelerator of almost 7-km circumference, consisting of six sextants, as illustrated in Fig. 1. Each sextant consists of a long straight section (LSS) and two arcs, at the two sides of the LSS. The accelerator is organized in 2 × 108 half-periods (determined by the main quadrupole locations), each of ∼32-m extension. Every sextant contains 36 half-periods—eight attributed to the LSS and 14 to each of the arcs. Assuming that X denotes the sextant's number $(1, \ldots, 6)$, the Arc−, LSS, and Arc+ would span over half-periods X00–X13, X14–X21, and X22–X35, respectively. Based on Sextant 1, this convention is illustrated in Fig. 2. Furthermore, within this work, the naming is such that ArcNM would contain both arcs (Arc$N$+ and Arc$M$−) between LSSN and LSSM.

Each LSS poses a specific functionality related to the accelerator operation. In LSS1, the beam is injected and scraped (cleaned from off-momentum particles). In LSS2, the beam is slowly extracted (i.e., over multiple turns) toward the TT20 beamline, which supplies particles to Fixed Target experiments in the North Area. LSS3 houses the radio frequency cavities responsible for the beam bunching and acceleration. Then, in both LSS4 and LSS6, the beam is fast extracted (i.e., within a single turn) toward the LHC or the SPS experiments. In the case of LSS4, through the TT40 extraction line, the beam is provided both to the counterclockwise circulating beam of the LHC and to the AWAKE experiment [2], whereas LSS6, via TT60 transfer line, supplies the beam to the clockwise-circulating beam of the LHC and the HIRADMAT facility [3]. Finally, as of 2021, LSS5 hosts the internal beam, which allows for a safe abort of the beam from the ring.

B. Operation

The SPS accelerator operates in cycles, each one lasting between a few and a few tens of seconds, depending on the beam user. The main beam users correspond to SFTPRO (Fixed Target experiments in the North Area), LHC, and HiRadMat. The examples of the SPS cycles for the most common beam users are depicted in Fig. 3.

Each year, the majority of the injected protons are sent to the North Area Fixed Target experiments (more than 85%), with the rest being shared mainly between LHC and HiRadMat

TABLE I
STATISTICS OF THE I.I.S TO THE SPS WITH THE BREAKDOWN AMONG THE MAIN BEAM USERS

	Unit	SFTPRO	LHC	HiRadMat	other
Typical Injected Intensity (I.I.)	10^{13}p	3.5-4	3-3.8	3-3.8	-
Typical Cycle Duration	s	10	22	22	-
Momentum at Injection	GeV/c	14	26	26	-
Momentum at Extraction	GeV/c	400	450	440	-
Total I.I. 2017	10^{17}p	141.7	7.5	2.0	0.9
Total I.I. 2018	10^{17}p	186.1	8.0	0.5	0.8
Total I.I. 2021	10^{17}p	105.0	0.4	4.1	7.9
Total I.I. 2022 until 17.05 (TS1)	10^{17}p	9.7	4.6	0.03	6.0
Total I.I. 2022 until 13.09 (TS2)	10^{17}p	156.2	9.3	0.13	6.1

TABLE II
SUMMARY OF THE SPS RADIATION MONITORS AND DOSIMETERS WITH THEIR MAIN PROPERTIES. POSITIONING OF THE BLMS REFERS TO THE ARC SECTORS (S.—SIDE BLM AND B.—BOTTOM BLM), AS SEVERAL MONITORS IN THE LSSS HAVE NONSTANDARD LOCATIONS

	DOFRS	BLM	RadMon	RPLs
# of units	continuous	269	59	varies
Spatial res.	≥ 1 m	discrete	discrete	discrete
Time res.	∼day	∼5 ms (as of 2021)	∼hour	passive
In operation	>=2021	>20 years	since 2016	2022
Distance (m): Horiz./Vert.	-1/-0.1	0.3/0 (s.) 0/-0.3 (b.)	0/-0.7	0/-0.7 +extra
Measurable	TID (SiO_2)	TID (air)	TID (SiO_2), 1-MeV-Si-n-eq, HEH-eq th-n-eq	TID (H_2O)

[a few percent of the annual injected intensity (I.I.)]. The statistics of the cycles and related intensities are listed in Table I.

C. Radiation Monitoring

Due to the complex and dynamic nature of the mixed-field radiation environment in the SPS accelerator, various complementary radiation monitoring devices have been deployed, especially in the locations where beam losses are expected. Given a large number of units and the related data size, automated processing had been put in place [18].

The radiation sensors are described in the following paragraphs, with the main properties summarized in Table II. Most of them are installed in a periodic manner in each arc period, with the representative positioning example depicted in Fig. 4.

All of them measure TID, with RadMon measuring additionally the relevant particle fluencies. However, given the varying sensitive materials and different calibration fields (e.g., ^{60}Co or charged hadron field), some discrepancy among the various TID monitor types due to differences in mixed-field response is expected.

1) Beam Loss Monitor: The beam loss monitoring system in the SPS consists of approximately 270 BLM units [8], ionization chambers filled with air, distributed along the entire accelerator in the locations with potentially high beam losses, and, therefore, high radiation levels. The system is, however, different with respect to the one installed in LHC [19]. Although the main purpose of the system is machine protection rather than dosimetry, it plays an essential role in the active monitoring of the radiation environment, mainly because of its very good time resolution (5 ms).

2) DOFRS: As of 2021, the SPS is entirely covered by the DOFRS providing the radiation profile along the cable tray, similarly as for the smaller CERN accelerators: the proton synchrotron and the proton synchrotron booster [20]. It measures the TID in the p-doped radiation-sensitive silica fiber based on the radiation-induced attenuation mechanism [21], [22]. Because of the active readout system [6], [23], not only annual spatial dose distribution can be retrieved, but also its time evolution. The system is deployed along the entire accelerator. In the arc sectors, the position of the sensor is constant transversely and follows the cable tray at the outer wall. In the LSSs, the position of fiber varies.

3) RPL Dosimeters: Prior to the DOFRS deployment, the TID along the accelerator was measured mainly by RPL dosimeters [7], [24], distributed along the SPS ring. Despite being a passive system, the RPL dosimeter outperforms other considered radiation monitors in terms of the TID (H_2O) measurement dynamic range, spanning between 0.1 and $\sim 5 \times 10^6$ Gy. During the 2022 operation, additional RPL dosimeters were deployed to do the following: 1) study the TID levels at the electronic equipment positions and 2) investigate the attenuation coefficients between the cable tray and the equipment level. Similar studies were performed in 2017 and 2018 using commercial nMOS transistors (deployed as dosimeters) [25]. However, in those years, DOFRS was not available.

4) RadMons: In addition to the four described systems, in the SPS arc sections, several units of COTS-based detectors, i.e., RadMons [9], [10], have been deployed. The main advantage is the capability of measuring not only TID (SiO_2), but also other quantities, such as high-energy-hadron-equivalent, 1-MeV-silicon-neutron-equivalent, thermal-neutron-equivalent fluencies, relevant for characterizing radiation environment with the focus on its effects on electronics. However, the RadMon system does not fully cover the needs related to the ALPS system radiation level monitoring due to differences in longitudinal positions along the accelerator and a limited number of deployed modules.

D. Prompt Radiation Sources

In the SPS sectors, the occurring beam loss mechanisms are not only determined by the amount of I.I. and the beam energy, but also by the beam user, and, therefore, by both the related beam and accelerator parameters. The most relevant beam loss mechanisms, in terms of radiation levels, are listed below.

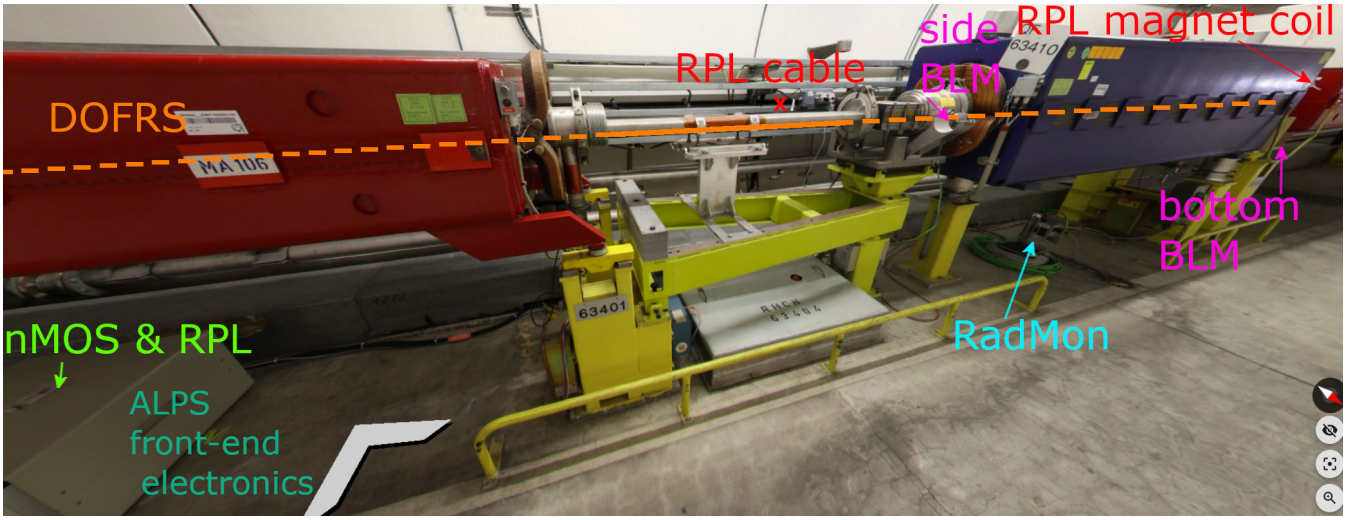

Fig. 4. Standard positions of the radiation sensors in the SPS arc sections, with the electronic rack of the ALPS system (with nMOS dosimeter on top, ∼0.9-m distance from the beamline), directly exposed to the mixed-field radiation. Behind the magnets, at the cable tray (∼1.3-m distance), as of 2021, the DOFRS monitor is installed. Before 2021, the TID was assessed by the RPL dosimeters (∼1-m distance), in each arc half-period one installed at the cable tray, and one at the magnet coil. Each arc half-period contains one BLM, installed either at the side of the beamline (∼30-cm distance) or under the first dipole magnet, as in the presented location. In addition, in some half-periods, RadMons are deployed under the magnets.

Following the occurrence in the cycle, the first losses will happen at the injection, as the shape of a batch from PS is not entirely matching the SPS RF buckets [26]. The parts of the beam that were not captured into RF buckets, so-called uncaptured beam, drift along the RF buckets [11], populating the kicker gap and leading to additional losses when kicker magnets are switched on, i.e., at fast extraction or successive injections. However, the majority of the uncaptured beam is lost at the very beginning of acceleration. Another example of a mechanism related to off-momentum losses is the transition crossing, happening only for SFTPRO cycles due to lower injection energy. As depicted in Fig. 5, the related beam losses during 2022 corresponded to 1.1% of the total I.I.

The other set of mechanisms is related to the transverse properties of a beam, in terms of physical dimensions, as the aperture of the beamline is limited. In particular, in the SPS, the vertical aperture is smaller as compared with the horizontal one, and several bottleneck locations were identified [27]. Apart from the aperture, other factors affecting the losses are optics functions ($\beta_{x,y}$ and dispersion D_x), determined by the magnet properties. In addition to the beam emittance, these functions have a direct impact on the macroscopic beam size.

Along the energy ramping, and despite the decreasing beam's emittance (a parameter that links the optic functions with the physical transverse shape of a beam), the impact of dispersion is increasing. This might lead to beam losses, particularly in the locations where the local maxima of dispersion function coincide with the aperture limitations.

After the completed acceleration, beam losses during the extraction are foreseen. Once the slow extraction starts, we excite a resonance and increase the beam shape to shave it deliberately using an electrostatic septum, which by design touches the beam and induces beam loss in LSS2, leading to high radiation levels in the LSS2 and several following periods. The extraction toward North Area takes place of several 100 000 turns.

The beam losses during the fast extraction are significantly lower. In the gap between the bunched beams, the fast pulsed magnets rise and extract the beam within a single turn.

Several other beam loss mechanisms are present during the SPS operation. An example of such is the interaction of the beam with the residual gas molecules that are present in the vacuum chamber. This mechanism is dominant in the LHC arc sectors; however, despite the lower vacuum quality in the SPS, the other beam loss mechanisms induced by beam-machine interactions (particularly those occurring at low energy) overshadow the residual-gas contribution.

The detailed analysis of beam loss mechanisms is outside the scope of this work, and the loss mechanisms are indirectly investigated by means of measured radiation levels, particularly with respect to their occurrence in SPS cycles. As the losses in the SPS energy regime are initiated by inelastic interactions, higher beam energy leads to more radiation showers and, therefore, higher radiation levels per unit lost proton. However, the measurements of TID are not directly proportional to the amount of beam losses.

To illustrate when the losses occur, the main cycles (SFTPRO, and LHC that is analogous to the HiRadMat) were divided, with respect to the beam momentum, into *injection*, *acceleration*, and *top energy* periods. In addition, for SFTPRO cycles, within *acceleration* period, a *transition* crossing subperiod has been defined.

Figs. 5 and 6 represent the normalized beam intensity decrease rate, due to beam losses/extraction/dump. To visualize how the related losses impact radiation levels, the plots are supported by normalized dose rate measurements from BLMs along the ring.

It is expected that the majority of TID related to beam losses due to uncaptured beam occur within the *injection* period or

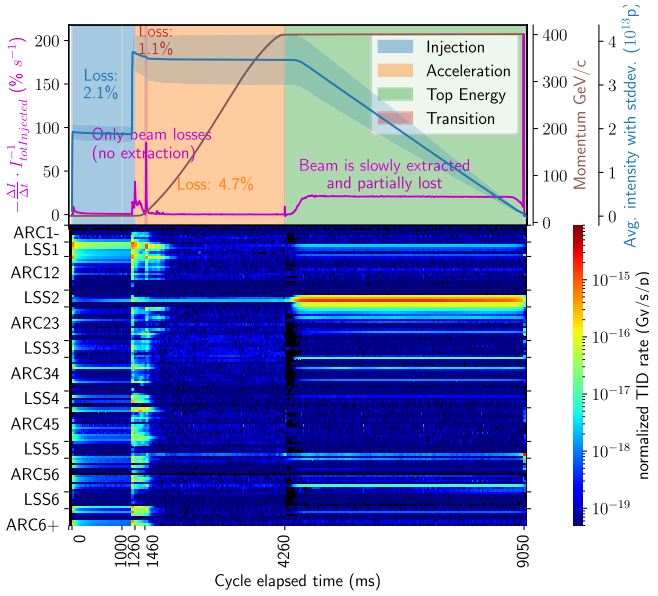

Fig. 5. Intensity loss rate normalized to the total I.I., as measured in 2022 during SFTPRO cycles. The loss rate includes lost, extracted, and dumped protons. For comparison purposes, the beam momentum, together with an averaged beam intensity and its standard deviation, is depicted. Only cycles with at least 10^{13} protons injected were considered. In these cycles, 2.1% of the total I.I. was lost in the machine during the *injection* period and 4.7% during the *acceleration* phase (including 1.1% lost at *transition* crossing). The bottom plot illustrates the I.I. normalized dose rate values along the accelerator as measured by the side BLMs in 2022 (until 13.09) during SFTPRO cycles.

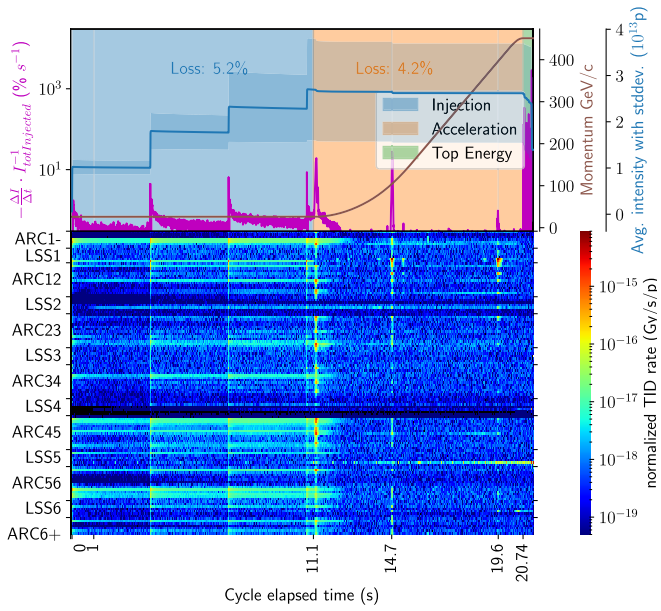

Fig. 6. Intensity loss rate normalized to the total I.I., as measured in 2022 during LHC cycles. The loss rate includes lost, extracted, and dumped protons. For comparison purposes, the beam momentum, together with an averaged beam intensity and its standard deviation, is depicted. Only cycles without dump occurring before the *top energy* period were considered. In these cycles, 5.1% of the total I.I. was lost in the machine during the *injection* period and 4.2% during the *acceleration* phase (at the very beginning of acceleration due to uncaptured beam, and during the beam scrapping at 14.7/19.6 s.). The bottom plot illustrates the I.I. normalized dose rate values along the accelerator as measured by the side BLMs in 2022 (until 13.09) during the LHC cycles.

at the very beginning of the *acceleration* period. This is the main beam loss mechanism for the LHC beams. The expected exceptions are as follows: 1) LSS1, where the beam is scraped; 2) LSS5, where the beam is safely removed at the dump; and 3) LSS4, where the beam is fast extracted toward the LHC. As LSS6 also supplies a beam to the LHC, an open point is the lack of a similar trend; i.e., the losses at the *top energy* are not observable. One of the explanations could be a different BLM positioning.

For SFTPRO beams, as expected, the mean TID measured in LSS2 (beam extraction) and LSS5 (safe beam disposal) are dominated by the *top energy* period. In addition, the arc sectors following these LSSs, i.e., 23 and 56, present analogous behavior, implying the impact of LSS functionality on the radiation levels seen in the following arcs.

III. Overview of Measured Radiation Levels

Prompt radiation levels encountered in the SPS span over several orders of magnitude, with annual measurements below 0.1 Gy and up to 1 MGy. In addition to both the longitudinal and the transverse position along the ring, the levels depend, to a lesser extent, on the material in which the dose is deposited.

A. Long Straight Sections

In LSS1, during 2022 operation, the highest radiation levels, reaching several tens of kGy, have been measured close to the beam momentum scraper (period 117–118), responsible for intercepting off-momentum particles, and close to the internal dump block (half-period 114) likely due to horizontal aperture bottleneck. In the LSS2, the radiation levels, reaching several hundreds of kGy, are mainly caused by the particles that are lost during the process of the slow-beam extraction, as depicted in Fig. 5.

LSS4 and LSS6 are analogous with each other in terms of the expected dominating radiation source term, which is the loss of the particles during fast extraction to the LHC, HiRadMat, or AWAKE. However, as depicted in Fig. 6, this is not the case, and the TID values in these LSSs are dominated by the losses due to the uncaptured SFTPRO beams, with the TID values reaching up to few hundreds Gy.

In LSS5, as of 2021, the dominating radiation source is the particle showers due to the disposal of beams on the dedicated beam dump, leading to TID levels up several tens of kGy.

B. Arc Sections

In the arc sections, the main magnets are arranged in a periodic manner, with one focusing quadrupole followed by four bending dipoles, one defocusing quadrupole, and four bending dipoles. These ten magnets constitute two arc half-periods (one period). Within the arc periods, the arrangement of the majority of radiation monitors (and passive dosimeters) resembles the main magnets' periodicity.

As opposed to the LHC [28], in the SPS arc sectors, the interactions of the residual gas with a beam are not the dominating loss mechanism. If that was the case, in the

presented TID breakdowns (Figs. 5 and 6), the majority of contribution in the arc sectors would come from the top energy (for SFTPRO) and acceleration (for LHC) periods, whereas, in all arc sectors, except sector 23, the majority of the losses occur at *injection* or early acceleration, likely due to uncaptured beam. Moreover, the impact of the LSS1/LSS2 functionality (scrapping/slow extraction), by means of similar loss occurrence within a cycle, can be observed in several locations along the machine.

An example of the TID measurements performed by the DOFRS in 2021 and 2022 is illustrated in Fig. 7, together with the TID estimates at the ALPS front-end racks, that will be covered in Section IV-B. Supporting DOFRS measurements with the BLM measurements allow for a detailed analysis of radiation peaks, particularly by means of their origin and time evolution.

Multiple other radiation peaks have been identified, particularly in arc sectors 12 (periods: 122–124 and 128), 45 (422–425), and 61 (622–626, 632–634, and 113), and are depicted in Fig. 8. The maximum measured TID values, at the arc cable tray, exceed 800 Gy, as measured by DOFRS with 1-m spatial resolution in half-period 113 during 2022. Whereas the BLMs are installed at the same positions in each half-period, it can be observed that those values are not linearly proportional to the DOFRS measurements, due to the following: 1) local shielding (e.g., from corrector magnets); 2) different loss mechanisms; and 3) issues (e.g., calibration) with either of the monitors.

Studies of the arc radiation environment are critical for the protection of the electronic systems (particularly ALPS front-end boards, described in Section V) to estimate the TID levels that the equipment encountered. As covered in detail in Section IV-B, the radiation levels measured in nearby locations are used in combination with empiric and/or simulation scaling factors to estimate the TID directly at the equipment position. The passive dosimeters provide accurate TID measurements, and the spatial pattern of the localized TID peaks strongly depends on accelerator parameters, and therefore, only active monitoring systems allow for instantaneous mitigation actions related to electronics protection.

IV. Correlations Between Radiation Monitors

As presented, the losses in the SPS arc happen due to various mechanisms, hence leading to different radiation showers and, therefore, varying composition of the mixed-field radiation. In addition, the available monitors and dosimeters were calibrated in the different reference fields (charged hadron versus ^{60}Co), with the TID given in various materials (air versus H_2O). On top of that, the different sensitive materials (SiO_2, air, and silver-activated phosphate glass) could lead to different responses in the mixed field. Within the scope of this article, the TID measurement from different sensors is compared to quantify the observed differences, knowing that some of them might be due to the above reasons, and at the same time demonstrate the capabilities of each sensor.

An example of the TID measurements over time is depicted in Fig. 9, for the BLMs, RadMon, and DOFRS. The relative time evolutions are in very good agreement, proving that DOFRS can be used not only for dosimetry but also for machine operational aspects, despite worse time resolution, as compared with the BLMs and RadMons. Whereas BLMs and RadMons allow to measure the TID levels only in the vicinity of arcs' quadrupole magnets, the DOFRS allows to detect TID levels at the bending dipoles, e.g., due to aperture restrictions. The multiplication factors vary among various locations due to the following: 1) differences in the radiation showers (beam loss mechanism and energy); 2) differences in local shielding due to corrector magnets; 3) uncertainty related to spatial mapping of the DOFRS; and 4) available spatial resolution. The scaling factors, although varying among locations, are fairly constant over time, which indicates that DOFRS TID measurement can be used for the assessment of the TID at various longitudinal locations, provided that the scaling factors in a location of concern are established, and no significant change (e.g., energy) in beam loss mechanism is observed.

TABLE III

TID Measured by BLMs, RPL Dosimeters, and DOFRS in the Selected SPS Half-Periods During a Fraction of 2022 Operation. The DOFRS Measurements Are Acquired With the 1-m Spatial Resolution and Averaged Over ±3 m From the RPL Pointwise Measurement, With Both Minimum and Maximum TID Values Reported. Except for the Last Row With the Bottom BLM, the Measurements Are Given at Two Transverse Locations: Cable Tray (DOFRS and RPL) and Beamline (BLM and RPL)

half-period	RPL TID (Gy in H_2O) at BLM	BLM TID (Gy in air)	RPL TID (Gy in H_2O) at cable	DOFRS TID $\text{avg}^{\text{max}}_{\text{min}}$ (Gy in SiO_2)
423	334	351	84.3	53^{85}_{14}
431	61.4	69.3	8.7	2^{11}_{0}
511	109	163	31.9	16^{28}_{4}
633	631	622	66.8	25^{51}_{10}
634	1039	no side BLM	168	51^{91}_{16}
634	336	684 (bottom)	59.4	63^{91}_{37}

A. BLM and RPL Dosimeters

To cross-check BLM measurements, several RPL dosimeters were deployed during May 17, 2022–September 13, 2022 at the BLMs locations. Measurements by RPL dosimeters ranged between 4 Gy and 1 kGy, as depicted in Fig. 10. The mean agreement was 43%, with all measurements (except one outlier) agreeing within a factor of 2. The measurements by side BLMs are in better agreement with RPL measurements. One of the explanations could be the additional shielding from the bottom BLM itself, due to different RPL-BLM arrangements. Unless explicitly mentioned, those BLMs were excluded from the analysis, as follows: 1) they show worse agreement with the RPL dosimeters and 2) due to a larger distance from the electronics racks.

B. Sensors at the Equipment and the Cable Tray

As presented in Fig. 11, the TID profile at the floor resembles the profile at the cable tray, with varying attenuation

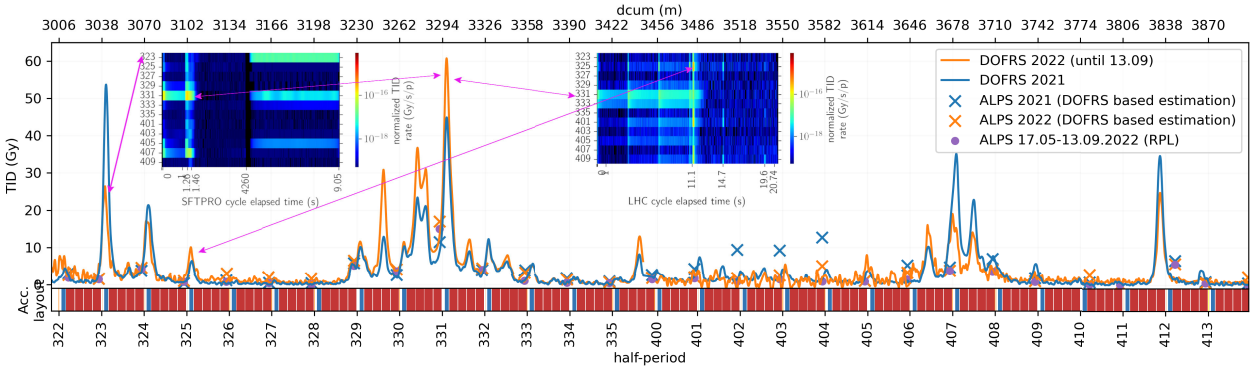

Fig. 7. TID (Gy in SiO_2, 2-m spatial resolution) in arc sector 34 as measured by DOFRS in the years 2021 and 2022 (until September), with the schematic magnet layout. In addition, the TID levels at the ALPS equipment are depicted, by means of RPL measurements from 2022, together with DOFRS-based estimates for 2021 and 2022. By focusing Figs. 5 and 6 on arc sector 34, the detailed radiation peak analysis can be performed. For example, in 2022, the peak in half-period 323 was due to North Area cycles, with the majority of the TID registered during the top energy. The peak in half-period 325 was driven by the LHC cycles and happened at the beginning of acceleration, likely due to the loss of the uncaptured beam. The peak in 331 is due to the SPS vertical aperture restriction [27], and the losses can be observed for both SFTPRO and LHC cycles.

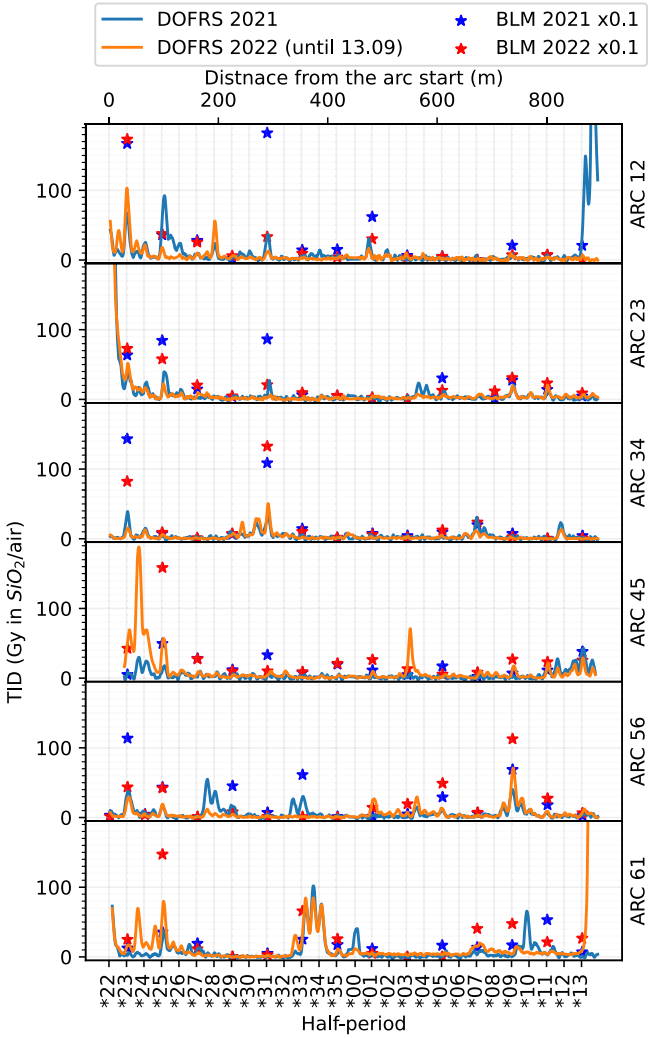

Fig. 8. TID along SPS arc sectors as measured in 2021 and 2022 (until September 13) by the DOFRS (dose in silica, 2-m spatial resolution) and BLMs (dose in air). For visibility purposes, the measurements by BLMs were divided by a factor of 10.

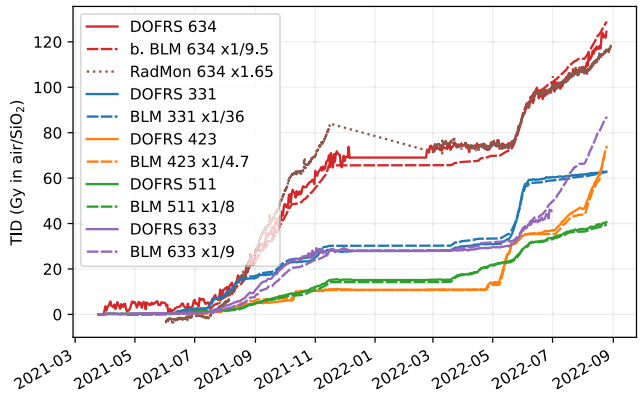

Fig. 9. Evolution of the TID over time as measured by DOFRS (Gy in SiO_2) and compared with the BLMs (Gy in the air) and RadMon measurements. The DOFRS trace is the mean TID measurement (acquired using with 2-m spatial resolution) from the BLM-corresponding longitudinal position extended by ±1 m. In half-period 634, the low-sensitive fiber had been used; therefore, the noise level is higher. The decrease of TID for the RadMON during the shutdown was due to the annealing effect.

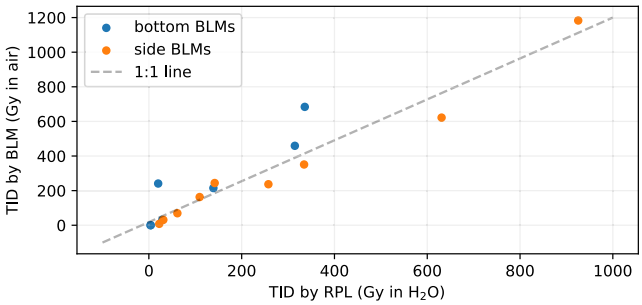

Fig. 10. TID as measured by the subset of BLMs (dose in air), installed both at the side and under the beamline, and RPL dosimeters (dose in H_2O), in May 17, 2022–September 13, 2022 period.

factors. Therefore, in case the direct measurement (by RadMon/nMOS/RPL) is not available, the ultimate goal of the DOFRS is to provide an estimate of the TID at the ALPS equipment, provided that the TID measured at the cable tray is known.

DOFRS TID measurements can be limited by the spatial resolution, in case a radiation peak has a physical extension, which is significantly shorter. Within this study, measurements

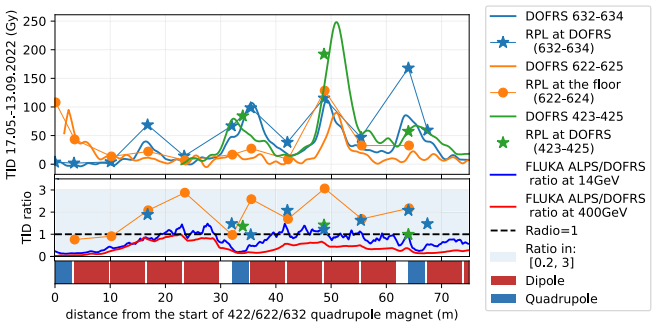

Fig. 11. TID levels along 423–424, 622–624, and 632–634 SPS half-periods as measured by DOFRS (cable tray, acquisition with 1-m spatial resolution), and RPL dosimeters on the floor (622–624) and the cable tray (423–425 and 632–634). The lower plot depicts the ratio between the TID measurements at the floor and at the cable tray (622–624) and between the TID measurements at the cable tray by RPL and by DOFRS (423–425 and 632–634). In addition, the simulated ratios between the ALPS (∼floor) and DORFRS (cable) are depicted, as retrieved via FLUKA Monte Carlo simulations for beam-residual gas losses happening at injection (14 GeV) and top energy (400 GeV), with the constant gas profile.

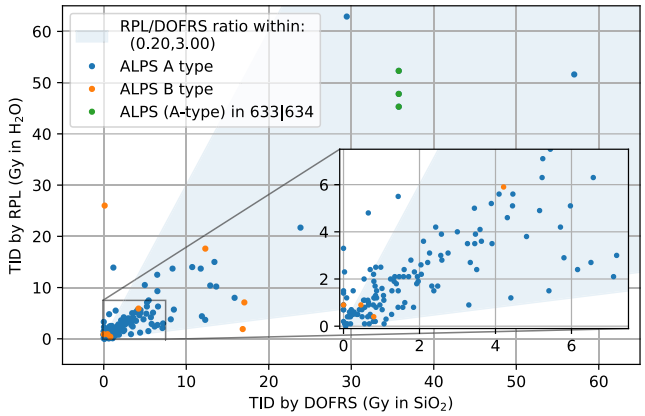

Fig. 12. TID at the ALPS racks as a function of the TID measured by optical fiber at the same longitudinal position (averaged over ±3 m). In the rack located at the end of half-period 633, in total three RPL dosimeters were installed, to estimate variability within a single unit (16%).

with 2-m spatial resolution are presented (unless mentioned otherwise). In several half-periods, the additional RPL dosimeters were deployed at the cable tray to do the following: 1) benchmark the past RPL measurements at the cable tray and 2) investigate the scaling factor (cable tray versus beamline) within the same sensor type (RPL). The measurements are reported in Table III and Fig. 11. Given the strong longitudinal TID gradients, a small systematic error in the longitudinal position might result in a significant error in the pointwise TID measurement. Therefore the table reports, in addition to the mean TID within ±3 m, both the minimum and maximum TID values within the considered longitudinal range. For 3/6 positions, the TID measured by both systems was in agreement, while considering the maximum DOFRS TID within ±3 m. The largest difference, as measured in half-period 634, was 85%, likely caused by aforementioned reasons related to the spatial nature of DOFRS, local shielding, not exactly the same vertical positions (up to 20-cm deviation), the difference in TID response at local mixed-field radiation, or systematic error larger than 3 m in the spatial mapping. As the DOFRS segments span over several hundreds of meters, the error of 3 m, in relative terms, would correspond to <0.5%.

In the fraction of 2022 operation, between 17.05 (TS1) and 13.09 (TS2), at the 92% of ALPS racks (167 units), the RPL dosimeters were installed. The remaining 15 units were not accessible due to the high activation level of the accelerator. Profiting from the very consistent (with BLMs and RadMons) time TID response (as shown in Fig. 9), RPL measurements were used to do the following: 1) retrieve the ALPS/cable coefficient ($\mathrm{RPL}_{\mathrm{TS1:2}}/D_{\mathrm{TS1:2}}$) for each electronic rack (given DOFRS parameters), to be used for the future/past TID estimation ($\mathrm{TID}_{\mathrm{ALPS}}$), together with the supporting DOFRS measurement ($D_{\Delta t}$) and 2) retrieve the distribution of the coefficients, to be used in the TID assessment, at the racks without deployed RPL dosimeters. The TID measurements by RPL dosimeters, as a function of the TID measured by the DOFRS, are illustrated in Fig. 12.

For the A-type-ALPS racks (B-type is a minority, 7% of racks) without an RPL measurement, and based on the spread of the coefficients, the proposed conservative coefficient is 3 (given the spatial resolution of 2 m, and averaging over ±3 m), as a majority of established A-type coefficients is below that value. The factor-3 coefficient is consistent with both the FLUKA-simulated and measured floor/cable ratios, depicted in Fig. 11. The FLUKA Monte Carlo simulation assumed a constant residual gas profile over half-periods 622–624. Due to the detection limit of the DOFRS, if the averaged measurement was $D_{\mathrm{TS1:2}} < 1$ Gy, the estimate has been performed based on factor 3. The procedure is summarized with the following equation:

$$\mathrm{TID}_{\mathrm{ALPS}}(\Delta t) = \begin{cases} D \equiv \mathrm{DOFRS} & \\ \dfrac{\mathrm{RPL}_{\mathrm{TS1:2}}}{D_{\mathrm{TS1:2}}} D_{\Delta t}: & \text{for } D_{\mathrm{TS1:2}} \geqslant 1 \text{ Gy} \\ 3 \cdot D_{\Delta t}: & \text{for } D_{\mathrm{TS1:2}} < 1 \text{ Gy} \\ 3 \cdot D_{\Delta t}: & \text{for } \mathrm{RPL}_{\mathrm{TS1:2}} \text{ undefined.} \end{cases} \quad (1)$$

V. Implications on Electronic Systems and RHA

In the CERN accelerator complex, radiation-safe areas for critical accelerator system containing active electronic components are defined as those with both a high-energy hadron fluence below 3×10^6 HEH/cm^2/year and a thermal neutron fluence below 3×10^7 n/cm^2/year. Above these levels, single event effects (SEEs) can pose a threat to the successful operation of the accelerator systems, especially in the case of those consisting of multiple radiation-exposed units (i.e., highly distributed systems) and for which a failure in a single unit results in the failure of the system as a whole, and, in turn, of the accelerator. Note that this limit is roughly a factor of 30 larger than the high-energy (>10 MeV) neutron flux at sea level, which is in the order of 1×10^5 n/cm^2/year.

An example of such a case is the negative impact on the SPS availability of soft errors in the accelerator access safety system in 2021 [17]. This system, despite being located in the side galleries of the accelerator, was exposed at

different locations to annual HEH fluence in the range of 10^7–10^8 HEH/cm^2/year, causing tens of beam aborts and associated accelerator downtime due to nondestructive SEEs in a commercial input–output PLC module. This system had to, therefore, be relocated to radiation-safe areas during the 2021–2022 end-of-year stop. The analysis of the HEH fluence measurements by RadMONs is, however, beyond the scope of this work.

Therefore, critical systems to be installed in non-radiation-safe areas in the CERN accelerator complex need to be SEE-tolerant, either by design (i.e., through in-house radiation-tolerant development and qualification, based mostly on COTS components) or through the radiation qualification of commercial electronics modules. However, the latter faces the key challenge of the traceability of the individual active semiconductor components used in these typically "black-box" modules.

Moreover, systems located in areas with radiation levels above 10^9 HEH/cm^2/year, corresponding to a dose rate of roughly 1 Gy/year, not only need to be robust to SEE, but also face the challenge of cumulative radiation effects (i.e., TID and displacement damage) on electronics. As shown in this article, the SPS accelerator tunnel, unlike the LHC, is exposed to such kind of levels in most (if not all) of its sectors. Whereas soft errors typically offer a variety of mitigation solutions (e.g., error-correcting code (ECC), scrubbing, triple modular redundancy (TMR), and other redundancy techniques), designing systems tolerant to cumulative effects is even more challenging, especially when considering lifetime TID values above a few hundred of Gy.

This is the case of the ALPS beam position monitoring (BPM) in the SPS, which is the result of a thorough radiation-tolerant design and qualification process. As demonstrated in its system-level test in CHARM (which constitutes the final step of CERN's RHA for accelerator systems), the radiation-exposed ALPS front end can withstand 750 Gy [29], albeit with a loss of functionality (notably the FPGA reprogramming capacity) at 200 Gy. Following the approach described in Section IV-B, the estimates of TID that the ALPS front end could encounter so far were retrieved and are depicted in Fig. 13. The values, in several locations, exceed the limit of 200 Gy. Finally, TID lifetime requirements in the order of a few kGy are highly unlikely to be met for nontrivial electronics boards and systems based on COTS components.

Therefore, the work of the radiation level characterization in the SPS needs to be seen in the context of the more global CERN RHA, notably in terms of categorizing the areas as R2E safe, COTS-based in-house designs requiring SEE tolerance, COTS-based in-house designs requiring SEE and cumulative damage tolerance, and exclusion of COTS-based system. Radiation monitoring is both essential for estimating the radiation levels a certain system will be exposed to, hence defining the related radiation tolerance targets for its design and qualification, as well as for actively measuring the levels during the operation of the system in order to, if applicable, preventively apply mitigation measures (e.g., relocation of a system exposed to larger radiation level than initially expected, or rotation of identical system units among positions with different radiation levels).

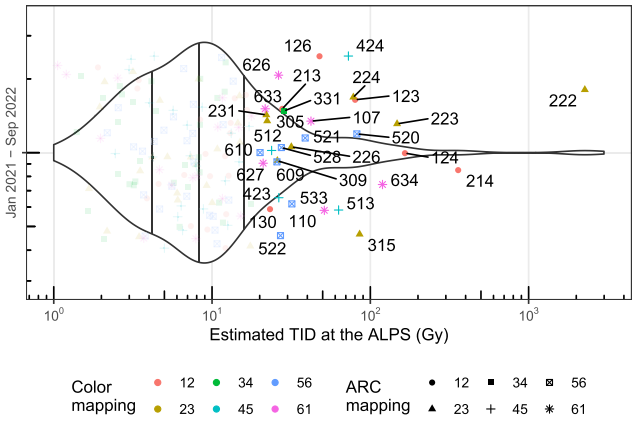

Fig. 13. Violin plot visualization of the estimated TID levels that ALPS front-end electronics could encounter so far. Vertical lines correspond to the first, second, and third quantiles. TID above 20 Gy was annotated with the half-period of concern (for racks at the very end of a period, the following period has been considered).

VI. Conclusion

This article addresses the problem of the radiation environment in the CERN SPS accelerator, particularly focusing on its arc sections, where COTS-based electronics is directly exposed to the accelerator's mixed-field radiation. Through the combination of different radiation monitoring techniques (optical fiber, RPL, and BLMs), the TID levels were analyzed, and their origin (beam loss mechanisms) was investigated. Although observed in the SPS, these mechanisms are present in all high-energy and high-intensity accelerators. Therefore, the presented analysis and methodology, relying on the synergy between different types of radiation monitors, not only contribute to the enhancement of the beam quality and efficiency in the CERN accelerator complex itself but also pave the way to the advancement in radiation monitoring in the current and future synchrotron accelerators throughout the world, for example, in the Brookhaven National Laboratory or in GSI/FAIR (SIS-18 or future SIS-100 accelerators).

One of the key achievements demonstrated in this work is the ability to measure the TID profiles over long distances (nearly 7-km coverage) through a dedicated DOFRS system. It can be exploited not only in other accelerator facilities but also used beyond accelerator applications, whenever there is a need for active and distributed radiation environment monitoring, for example, to monitor the neutron-induced TID in future moonbases.

It has been demonstrated that DOFRS measurements, in addition to their excellent spatial properties, successfully reflect the time evolution measured by nearby BLMs/RadMon. However, to investigate the origin of the losses and mitigate them if applicable, it is essential to use instruments with higher (ms) time resolution, such as BLMs. The comparison of TID measured by the different sensors (BLMs, RPLs, and DOFRS) yields the agreement within a factor of 2.

To address the challenge of providing the TID estimate directly at the electronic equipment, several additional passive RPL dosimeters were deployed directly on the electronics

racks to provide the following: 1) direct TID measurement and 2) a local scaling coefficient with the nearby radiation monitor, to be used to retrieve the TID estimate once the direct measurement is not available. It has been found that more than 75% of the units collect less than 20 Gy/year, although, in several locations, the estimated TID values reached up to 100 Gy/year, with the maximum value in the order of several hundreds of Gy/year.

As has been shown, radiation levels in the nearby alcoves are large enough to induce soft errors in industrial electronics, whereas levels in the tunnel call for custom electronics designs, mainly based on COTS and developed to be SEE-free, through a combination of part selection and fault tolerance and mitigation, and with TID limits in the order of several hundreds of Gy.

In both cases, active monitoring of the related radiation levels is crucial in order to implement preventive maintenance solutions, as well as to, when applicable, put in place mitigation actions for radiation effects impacting the overall performance of the accelerator.

ACKNOWLEDGMENT

The authors would like to thank V. Kain for the super proton synchrotron (SPS) operations insights and SY-BI-BL Section (particularly Christos Zamantzas and Ewald Effinger) for the support related to the beam loss monitor (BLM) system.

REFERENCES

[1] R. G. Alía et al., "LHC and HL-LHC: Present and future radiation environment in the high-luminosity collision points and RHA implications," *IEEE Trans. Nucl. Sci.*, vol. 65, no. 1, pp. 448–456, Jan. 2018.

[2] E. Adli et al., "Acceleration of electrons in the plasma wakefield of a proton bunch," *Nature*, vol. 561, no. 7723, pp. 363–367, Sep. 2018.

[3] I. Efthymiopoulos et al., "HiRadMat: A new irradiation facility for material testing at CERN," in *Proc. 2nd IPAC*. Geneva, Switzerland: JACoW Publishing, Nov. 2011, p. 1665.

[4] D. Banerjee (Jul. 2021). *The North Experimental Area at the CERN Super Proton Synchrotron*. Accessed: Sep. 1, 2022. [Online]. Available: https://cds.cern.ch/record/2774716

[5] L. Evans and P. Bryant, "LHC machine," *J. Instrum.*, vol. 3, no. 8, Aug. 2008, Art. no. S08001.

[6] D. Di Francesca et al., "Dosimetry mapping of mixed-field radiation environment through combined distributed optical fiber sensing and FLUKA simulation," *IEEE Trans. Nucl. Sci.*, vol. 66, no. 1, pp. 299–305, Jan. 2019.

[7] H. Vincke et al., "Response of alanine and radio-photo-luminescence dosemeters to mixed high-energy radiation fields," *Radiat. Protection Dosimetry*, vol. 125, pp. 340–344, Mar. 2007.

[8] C. Zamantzas et al., "System architecture for measuring and monitoring beam losses in the injector complex at CERN," CERN, Geneva, Switzerland, Tech. Rep. CERN-ACC-2013-0252, Aug. 2012. Accessed: Sep. 1, 2022. [Online]. Available: https://cds.cern.ch/record/1627308

[9] G. Spiezia et al., "The LHC radiation monitoring system—RadMon," *Proc. Sci.*, vol. 143, pp. 1–12, Jul. 2011.

[10] G. Spiezia et al., "A new RadMon version for the LHC and its injection lines," *IEEE Trans. Nucl. Sci.*, vol. 61, no. 6, pp. 3424–3431, Dec. 2014.

[11] G. Arduini. (Jan. 2017). *Report of the Beam Losses and Radiation Working Group*. Accessed: Sep. 1, 2022. [Online]. Available: https://edms.cern.ch/ui/file/1160274/2/BLRWG_Report_v14_GA.pdf

[12] M. Patecki, A. Mereghetti, D. Mirarchi, and S. Redaelli, "Conceptual design of an off-momentum collimation system in the CERN super proton synchrotron for high-luminosity large hadron collider proton beams," *Phys. Rev. Accel. Beams*, vol. 24, no. 9, Sep. 2021, Art. no. 093002.

[13] H. Bartosik and G. Rumolo, "Proceedings of the injector MD days 2017," CERN, Geneva, Switzerland, Tech. Rep. CERN-Proceedings-2017-002, Mar. 2017.

[14] G. Roy, "Radiation in the SPS," in *Proc. 10th Workshop LEP SPS Perform., Chamonix X*, Jan. 2000, pp. 52–55.

[15] R. Billen, "SPS remanent radiation: The warm spots," CERN, Geneva, Switzerland, Tech. Rep. CERN-ACC-NOTE-2019-0043, Mar. 1998. Accessed: Sep. 1, 2022. [Online]. Available: http://cds.cern.ch/record/702440

[16] A. Boccardi et al., "Commissioning of ALPS, the new beam position monitor system of CERN SPS," in *Proc. IBIC*, no. 10. Geneva, Switzerland: JACoW Publishing, Oct. 2021, pp. 96–99.

[17] Y. Aguiar et al., "Implications and mitigation of radiation effects on the CERN SPS operation during 2021," in *Proc. 13th Int. Part. Accel. Conf. (IPAC)*, no. 13. Geneva, Switzerland: JACoW Publishing, Jul. 2022, pp. 740–743.

[18] K. Biłko, R. G. Alía, and J. B. Potoine, "Automated analysis of the prompt radiation levels in the CERN accelerator complex," in *Proc. 13th Int. Part. Accel. Conf. (IPAC)*, no. 13. Geneva, Switzerland: JACoW Publishing, Jul. 2022, pp. 736–739.

[19] E. B. Holzer et al., "Beam loss monitoring system for the LHC," in *Proc. IEEE Nucl. Sci. Symp. Conf. Rec.*, vol. 2, Oct. 2005, pp. 1052–1056.

[20] D. D. Francesca et al., "Distributed optical fiber radiation sensing in the proton synchrotron booster at CERN," *IEEE Trans. Nucl. Sci.*, vol. 65, no. 8, pp. 1639–1644, Aug. 2018.

[21] D. Di Francesca et al., "Qualification and calibration of single-mode phosphosilicate optical fiber for dosimetry at CERN," *J. Lightw. Technol.*, vol. 37, no. 8, pp. 4643–4649, Sep. 15, 2019.

[22] D. Di Francesca et al., "Radiation-induced attenuation in single-mode phosphosilicate optical fibers for radiation detection," *IEEE Trans. Nucl. Sci.*, vol. 65, no. 1, pp. 126–131, Jan. 2018.

[23] D. Di Francesca, K. Kandemir, G. Li Vecchi, R. G. Alia, Y. Kadi, and M. Brugger, "Implementation of optical-fiber postmortem dose measurements: A proof of concept," *IEEE Trans. Nucl. Sci.*, vol. 67, no. 1, pp. 140–145, Jan. 2020.

[24] D. Pramberger, Y. Q. Aguiar, J. Trummer, and H. Vincke, "Characterization of radio-photo-luminescence (RPL) dosimeters as radiation monitors in the CERN accelerator complex," *IEEE Trans. Nucl. Sci.*, vol. 69, no. 7, pp. 1618–1624, Jul. 2022.

[25] M. Brucoli. (Jul. 2019). *TID, HEH and ThN Measurements Along the SPS Accelerator and the Adjacent Tunnel Access Areas*. Accessed: Sep. 1, 2022. [Online]. Available: https://cds.cern.ch/record/2693061

[26] M. Schwarz, H. Bartosik, E. Chapochnikova, A. Lasheen, J. Repond, and H. Timko, "Studies of capture and flat-bottom losses in the SPS," in *Proc. 61st ICFA Adv. Beam Dyn. Workshop (HB)*, no. 61. Geneva, Switzerland: JACoW Publishing, Jul. 2018, pp. 180–185, Paper TUP2WA03.

[27] V. Kain et al., "Identification and removal of SPS aperture limitations," in *Proc. 9th Int. Part. Accel. Conf. (IPAC)*, no. 9. Geneva, Switzerland: JACoW Publishing, May/Jun. 2018, pp. 709–712, Paper TUPAF021.

[28] K. Bilko et al., "Radiation environment in the LHC arc sections during run 2 and future HL-LHC operations," *IEEE Trans. Nucl. Sci.*, vol. 67, no. 7, pp. 1682–1690, Jul. 2020.

[29] M. B. Marin et al., "The Giga bit transceiver based expandable front-end (GEFE)—A new radiation tolerant acquisition system for beam instrumentation," *J. Instrum.*, vol. 11, no. 2, Feb. 2016, Art. no. C02062.